3D Numerical Modelling of Scour around a Jacket Structure with Dynamic Free Surface Capturing

Nadeem Ahmad*[1], Arun Kamath[1], and Hans Bihs[1]

[1]Department of Civil and Environmental Engineering, Norwegian University of Science and Technology (NTNU), 7491 Trondheim, Norway

Ocean Engineering, 2020, **200** , pp. 107104.
DOI: http://dx.doi.org/10.1016/j.oceaneng.2020.107104

Abstract

This paper presents a numerical investigation of local scour with dynamic free surface capturing around a jacket structure. The hydrodynamics and resulting scour are calculated using the open-source CFD model REEF3D. The model solves the Reynolds-averaged Navier-Stokes equations with $k-\omega$ turbulence closure. The free surface is captured with the level set method. The simulated flow hydrodynamics are coupled with sediment transport algorithms. The modelling of the local scouring process is based on the bed load and the suspended load while accounting for the bed slope for the calculation of the critical bed shear stress. In order to obtain a more realistic prediction of the scour hole, a sand-slide algorithm is implemented to correct the bed slope when it exceeds the angle of repose. The grid and time step size convergence tests are performed to ensure the quality of the simulated hydrodynamics in the numerical wave tank (NWT). The model is validated for local scour around a pile in an experimental flume using different values of Keulegan-Carpenter number (KC). The results show a good agreement with the experimental data. The validated model is applied to simulate scour around a jacket structure. The key findings from the study are the modelling of flow hydrodynamics and the time development of local scour around a jacket exposed to waves and steady current.

Keywords: CFD; REEF3D; jacket structure; wave induced scour; local scour; numerical wave tank; free surface; level set method

---

*Corresponding author,nadeem.ahmad@ntnu.no
Postprint, published in Ocean Engineering, doi:http://dx.doi.org/10.1016/j.oceaneng.2020.107104

1 Introduction

The offshore industry has to deal with increased renewable energy demand and the development of large jacket structures to support offshore wind turbines. Failure of a jacket can lead to high costs for repair and maintenance. Thus, the stability of a jacket is an important concern and needs to be analysed for the local scour and well as global scour around the jacket structure.

There is limited knowledge about the scouring process around jacket structures which is mainly gained through the field investigations and physical modelling (Van Dijk, 1980). Dahlberg (1983) studied scour around the gravity platforms and jacket structures. The observations showed that significant scour occurs mainly in areas with active sand waves. Rudolph et al. (2004) investigated scour around jacket structures in the southern North Sea. They demonstrated scour around structures exposed to the waves and current for a long duration. It was suggested that the mean scour development can be reproduced with the empirical formula by Nakagawa and Suzuki (1976). Bolle et al. (2012) discussed scour around a jacket structure at the C-Power wind farm at Flemish coast, to design protection measures. In a recent study, Stahlmann (2013) investigated scour around a tripod structure through laboratory experiments. In his study, the global and local scour and the effect of incident wave direction on scour around a tripod structure have been investigated.

These studies are found to be a challenging and time-consuming process as field measurements or complex laboratory experiments are involved. Alternatively, the maximum scour around a jacket can be calculated using empirical formulae from Sumer et al. (1992). The formulae calculate the scour depth around the vertical piles without accounting for the complexity of the structure. The calculation of the maximum scour depth around jacket structures using empirical formulae might result in unrealistic scour depths, as the scour process around a jacket cannot be represented thoroughly as one scour hole. To overcome this problem, CFD modelling of the scouring process around jacket structures can be a potential alternative way to analyse the scour problems more accurately.

Many researchers have studied local scour around the simple structures with CFD modelling approach. Mostly, these structures are vertical piles (Ahmad et al., 2015), horizontal piles (Ahmad et al., 2019*b*), abutments (Bihs and Olsen, 2011), seawalls (Ahmad et al., 2018*a*, 2019*a*), and a group of vertical piles (Ahmad et al., 2018*b*). Olsen and Kjellesvig (1998) investigated the scour around a circular cylinder exposed to a steady current. The study was performed by solving the Navier-Stokes equations coupled with sediment transport algorithms. A clear-water scour was simulated until an equilibrium state achieved. Tseng et al. (2000) studied the scour around both circular and square cylinders exposed to a steady current. The large eddy simulation (LES) approach was used to investigate the vortex shedding and sediment transport. Roulund et al. (2005) investigated the scour around a vertical pile exposed to a steady current. They investigated the influence of the boundary-layer thickness, Reynolds number, bed roughness and the scour processes. Baykal et al. (2015) investigated the flow and consequently the local scour around a vertical cylinder. They discussed the vortex shedding and sediment transport process. It was concluded that the equilibrium scour depth is reduced by 50% when the suspended load is not considered. Baykal et al. (2017) investigated the scour around a vertical pile exposed to wave. It was found that the local scour and backfilling are governed by the lee-wake flow. The equilibrium depth of the scour holes was seen to be the same for both the scour and the backfilling for a given Keulegan-Carpenter number.

However, in these studies, the free surface was not resolved. Liu and Garcia (2008) employed a three-dimensional numerical model to simulate the local scour around a vertical pile with free water surface capturing. Afzal et al. (2015) and Ahmad et al. (2015) investigated the scour around a large pile under a steady current and scour under a wave with a free surface. It was found that the scour depth and deposition increase with the Keulegan-Carpenter (KC $= 2\pi a/D$) number. Scour below the pipelines (horizontal pile) has been investigated by Liang and Cheng (2005); Fuhrman et al. (2014); Liu et al. (2016); Larsen et al. (2016). In these studies, scour beneath the submarine pipelines exposed to a steady current-alone, wave-alone and wave plus current. The backfilling processes and temporal variation of the scour were also discussed. However, the studies were found limited to 2D modelling of local scour with no free surface capturing. Ahmad et al. (2019*b*) presented a 2D numerical modelling of pipeline scour under a steady current, waves and the combined action of waves and current including the unsteady free surface. The results demonstrated the flow field below the pipeline, the scour depth and the temporal variation of the scouring process for different conditions of flow. Bihs and Olsen (2011) discussed local scour around an abutment exposed to a steady current. It was found that the reduction of the bed shear stress on a sloping bed improves the calculation of the local scour. Ahmad et al. (2018*a*, 2019*a*) presented modelling of scour due to wave impact on a vertical seawall. It was found that the seawall scour is governed by the breaking wave impact on the seawall and the development of the standing wave due to the reflected wave energy from the seawall leads to further sediment transport seawards. These studies provide investigations scour around simple structures. In case of a complex assembly of piles, Ong et al. (2013) developed a mathematical model for the local scour around the vertical piles placed in different arrangement exposed to the long-crested and short-crested nonlinear random waves plus a current. A stochastic method was provided to obtain the maximum equilibrium scour depth around the group of vertical piles. Ahmad et al. (2018*b*) investigated wave-induced scour around a side-by-side arrangement of piles with free surface capturing. The study examined the local scour around piles in a long and truncated domain. The study further elaborated on the factors affecting the local scour around the multiple piles such as the KC number and gap between the piles. In a recent study, Stahlmann and Schlurmann (2012) investigated scour around a tripod structure. The study discussed the wave field characteristics, scour evolution and the temporal variation of scour depth around a tripod structure. Although existing research provides a large amount of knowledge about local scour around the simple structures and a tripod, further study of scour around a jacket structure, which is a complex assembly of the vertical, horizontal and diagonal piles, has yet to be undertaken.

The primary objective of this study is to model the scour around a jacket structure with the free surface featuring. The model is employed to simulate scour for a real case scenario of scour around a jacket structure at C-power wind farm, Thornton bank at the Belgian coast (Bolle et al., 2012). Grid and time step size convergence studies are performed to ensure the quality of the simulated hydrodynamics in the numerical wave tank (NWT). The numerical model is then successively validated for scour around a vertical cylinder exposed to waves for different KC numbers. The successfully validated model is then applied to simulate scour around a jacket structure. In order to model a realistic scenario, the wave input and sediment bed properties are taken from the C-power wind farm. According to the available field data, waves of height 4.5 m were observed under storm conditions in January 2012 and resulted in a large amount of scouring around the jacket (Bolle et al., 2012). This scenario is studied using two simulations. The first simulation discusses the scour calculations for a wave of height

$H = 4.5$ m which represents the wave conditions observed during the storm at the site. As the scour depth increases with the KC number, another simulation is run for the scouring process under a steady current which corresponds to KC = ∞. For this case, the undisturbed depth-averaged inflow velocity is considered to be $u = 0.60$ m/s. The results discuss the complex hydrodynamics, the maximum scour depth, deposition, and the temporal variation of the scour process around the jacket structure.

2 Numerical Model

2.1 Hydrodynamic model

The open-source CFD model REEF3D (Bihs et al., 2016; Bihs and Kamath, 2017) is used for the numerical modelling of wave hydrodynamics and the local scouring process. The model solves the incompressible Reynolds-averaged Navier-Stokes (RANS) equations, involving the solution of the continuity and the momentum equations to calculate the flow and pressure field. The continuity and momentum equations are shown below:

$$\frac{\partial u_i}{\partial x_i} = 0 \tag{1}$$

$$\frac{\partial u_i}{\partial t} + u_j \frac{\partial u_i}{\partial x_j} = -\frac{1}{\rho}\frac{\partial p}{\partial x_i} + \frac{\partial}{\partial x_j}\left[\nu\left(\frac{\partial u_i}{\partial x_j} + \frac{\partial u_j}{\partial x_i}\right) - \overline{u_i u_j}\right] + g_i \tag{2}$$

where u_i is the fluid velocity, p is the pressure, ρ is the fluid density, ν is the fluid kinematic viscosity, g is the gravitational acceleration and $\overline{u_i u_j}$ is representing the Reynolds stresses. The RANS equations are closed by replacing the Reynolds stresses with the boussinesq-approximation as:

$$-\overline{u_i u_j} = \nu_t\left(\frac{\partial u_i}{\partial x_j} + \frac{\partial u_j}{\partial x_i}\right) + \frac{2}{3}k\ \delta_{ij} \tag{3}$$

$$\nu_t = k/\omega \tag{4}$$

where ν_t is the eddy viscosity, k is the turbulent kinetic energy density, ω is the specific turbulent dissipation rate. The kronecker delta δ_{ij}= 1 for i = j, otherwise $\delta_{ij} = 0$. The k-ω model (Wilcox, 1994) is used to calculate the eddy viscosity ν_t by solving for the partial differential equations for the turbulent kinetic energy density k and the specific turbulent dissipation rate ω. The equations for k and ω are defined as:

$$\frac{\partial k}{\partial t} + u_j \frac{\partial k}{\partial x_j} = \frac{\partial}{\partial x_j}\left[\left(\nu + \frac{\nu_t}{\sigma_k}\right)\frac{\partial k}{\partial x_j}\right] + P_k - \beta_k k\omega \tag{5}$$

$$\frac{\partial \omega}{\partial t} + u_j \frac{\partial \omega}{\partial x_j} = \frac{\partial}{\partial x_j}\left[\left(\nu + \frac{\nu_t}{\sigma_\omega}\right)\frac{\partial \omega}{\partial x_j}\right] + \frac{\omega}{k}\alpha P_k - \beta\omega^2 \tag{6}$$

Where, P_k is the turbulent production rate which is described as follows:

$$P_k = \nu_t \frac{\partial u_i}{\partial x_j}\left[\frac{\partial u_i}{\partial x_j} + \frac{\partial u_j}{\partial x_i}\right] \tag{7}$$

The remaining coefficients in equation (4) are taken as follows: α=$\frac{5}{9}$, $\beta_k = \frac{9}{100}$, β=$\frac{3}{40}$, $\sigma_\omega = 2$ and $\sigma_k = 2$. The overproduction of the turbulence in a highly strained flow outside the boundary layer (Durbin, 2009) is managed as follows:

$$\nu_t = \min\left(\frac{k}{\omega}, \sqrt{\frac{2}{3}}\frac{k}{|\mathbf{S}|}\right) \tag{8}$$

where $\mathbf{S}$ is the mean strain rate:

$$S_{ij} = \frac{1}{2}\left(\frac{\partial u_j}{\partial x_i} + \frac{\partial u_i}{\partial x_j}\right) \tag{9}$$

In the vicinity of the walls, the turbulence parameters are calculated using the wall laws as:

$$u^+ = \frac{1}{\kappa}\, ln\left(\frac{30y}{k_s}\right) \tag{10}$$

where u^+ is the dimensionless wall velocity, $\kappa = 0.4$ is the von Karman constant, y is the water depth and k_s is the equivalent sand roughness. It is assumed that the turbulent production is equal to the turbulent kinetic energy density dissipation near the wall (Wilcox, 1994). The value of the specific turbulent dissipation for a distance Δy_p from the wall to the center of the bed cell is given as:

$$\omega_{wall} = \frac{c_\mu^{3/4} k_w^{1/2}\; U_w^+}{\Delta y_p} \tag{11}$$

where $c_\mu = 0.09$ is the model cofficient. The turbulent kinetic energy k at the wall is treated by integrating the source terms of Eq.(5) over the bed cell:

$$\int (P_k - \epsilon_{wall})\rho = \left[\frac{\tau_w U_w}{\Delta y_p} - \frac{\rho c_\mu^{3/4} k_w^{3/2} U_w^+}{\Delta y_p}\right] \tag{12}$$

The value for the wall shear stress τ_w and the dimensionless wall velocity U_w^+ is obtained from rough wall law. Away from the wall, the value of the eddy viscosity is estimated by the formulation in Eqs. (5-9). The RANS models are seen to be unstable in the potential flow region leading to an unphysical turbulent kinetic energy and eddy viscosity (Larsen and Fuhrman, 2018; Jacobsen et al., 2012). Additionally, high-velocity gradients around the free surface generate overproduction of turbulence that causes an artificial damping of the free surface. In this paper, the method suggested by Naot and Rodi (1982) is used to manage the overproduction of the turbulence at the free surface. Details of the method can be found in Kamath et al. (2019).

2.2 Numerical wave tank and free surface model

The waves are generated in a 3D NWT. The inlet of the NWT is specified with the Dirichlet type inlet boundary condition where the incident wave velocity is prescribed based on the chosen wave theory. The waves are absorbed with the active wave absorption method (AWA)

(Higuera et al., 2013) at the outlet where the reflected waves from the outlet are cancelled using the negative value of the corrected velocity u_c, which is described as follows:

$$u_c = -\sqrt{\frac{g}{h}}.\eta_r \tag{13}$$

where u_c is the corrected velocity, h is the still water depth, g is the gravitational acceleration, and η_r is the reflected wave amplitude which is defined as:

$$\eta_r = \eta_m - \eta_g \tag{14}$$

where η_m is the measured free surface elevation, η_g is the generated free surface. The method is considered to be a good choice to manage both the wave generation and the absorption in a relatively short numerical wave tank (Ahmad et al., 2018*b*). The bottom of the NWT is considered as a no-slip wall and the top of the NWT is considered to be a symmetry plane. On the surface of the structure, a no-slip wall boundary condition is imposed. The sediment bed is treated with a rough-wall function where a logarithmic wall function is applied in order to account for the bed roughness.

The free surface is captured using the level set method (Osher and Sethian, 1988). This method uses a continuous signed distance function $\phi(\vec{x}, t)$ to represent the interface between two immiscible fluids. The interface is computed under the velocity field u_j. The level set function is zero on the interface, the positive distance from the interface is phase 1 and the negative distance from the interface is calculated to be phase 2. This is defined as follows:

$$\phi(\vec{x}, t) \begin{cases} > 0 & if\ \vec{x}\ is\ in\ phase\ 1 \\ = 0 & if\ \vec{x}\ is\ at\ the\ interface \\ < 0 & if\ \vec{x}\ is\ in\ phase\ 2 \end{cases} \tag{15}$$

The propagation of the level set function $\phi(x, t)$ is calculated solving the convection equation as follows:

$$\frac{\partial \phi}{\partial t} + u_j \frac{\partial \phi}{\partial x_j} = 0 \tag{16}$$

The convective velocity u_j is calculated from the solution of the RANS-equations and transforms the level set function in space and time. As the free surface evolves, the level set function $\phi(\vec{x}, t)$ loses its signed distance property. Therefore, the level set function $\phi(\vec{x}, t)$ is reinitialised after each time step (Peng et al., 1999).

2.3 Morphological model

The modelling of the local scouring process is based on the calculation of the bed shear stress due to the velocity field from the hydrodynamic model. The logarithmic wall function is applied to calculate the bed shear stress as follows:

$$\tau = \rho u_*^2 \tag{17}$$

where u_* is the shear velocity and is defined as:

$$\frac{u}{u_*} = \frac{1}{\kappa}\ ln\left(\frac{30.2z}{k_s}\right) \tag{18}$$

Here, u is the water velocity at a height z above the bed, $\kappa = 0.4$ is the von Karman constant, $k_s = 3d_{50}$ is the equivalent sand roughness and d_{50} is the median grain size. The initiation of the sediment transport takes place when the simulated bed shear stress (τ) exceeds the critical bed shear stress τ_c. The sediment mobility is calculated in terms of the bed load and the suspended load. The calculation of the bed load is made with van Rijn's (van Rijn, 1984*a*) formula as follows:

$$\frac{q_B}{d_{50}^{1.5}\sqrt{(s-1)g}} = 0.053\ \frac{T^{2.1}}{D_*^{0.3}} \tag{19}$$

Here, $T = (\tau - \tau_{cr})/\tau_{cr}$ is the transport stage parameter, $D_* = d_{50}\left[\frac{(s-1)g}{\nu^2}\right]^{1/3}$ is the particle parameter, τ_{cr} is the modified Shields critical bed shear stress, $s = \rho_s/\rho$ is the specific density, ρ_s is the sediment density and ρ is the water density. The modified critical bed shear stress is calculated using the formulation suggested by Dey (2003). The effect of the sloping bed is accounted for by considering the longitudinal bed slope θ, the transverse bed slope α, the angle of repose of the sediment φ and the drag and lift forces, yielding the expression for the critical bed shear stress modification factor r. The modified critical bed shear stress τ_{cr} is then calculated from τ_0 obtained from the standard Shields diagram (Shields, 1936):

$$\tau_{cr} = r\ \tau_0 \quad \text{and} \quad \tau_0 = \theta_c\ (s-1)\ \rho g d_{50} \tag{20}$$

where θ_c is the critical shields parameter. The critical bed shear stress τ_0 is calculated based on $\theta_c = 0.05$. Different angles of repose are considered for the uphill and downhill slopes in the sandslide algorithm following the observations from the experiments by Lysne (1969*a*), where the calculated angle of repose on slopes in the direction of flow was found to be much higher than the angle of internal friction. This effect was seen to be higher for steeper slopes.

The suspended sediment load is calculated using a convection-diffusion equation. The numerical treatment for this transport equation is performed in a similar fashion as for the momentum equations.

$$\frac{\partial c}{\partial t} + u_j\frac{\partial c}{\partial x_j} + w_s\frac{\partial c}{\partial z} = \frac{\partial}{\partial x_j}\left(\Gamma\frac{\partial c}{\partial x_j}\right) \tag{21}$$

Here, c is the suspended load concentration, Γ is the sediment mixing coefficient, and w_s is the fall velocity of the sediment particles which is calculated based on the Stokes law. The value of Γ is assumed to be equal to the eddy viscosity (Hunt, 1954). The solution of this equation is determined by setting as boundary conditions zero vertical sediment flux at the free surface and the bottom suspended load concentration (c_b) as calculated from van Rijn (1984*b*) formula:

$$c_b = 0.015\frac{d_{50}}{a}\left(\frac{T^{1.5}}{D_*^{0.3}}\right) \tag{22}$$

where a is the reference level for the suspended load. In the present model, the reference level is assumed to be equal to the equivalent-roughness height as $k_s = 3d_{50}$. The sediment concentration close to the bed is interpolated using the Rouse (1937) equation:

$$c(z) = c_b\left(\frac{h-z}{z}\frac{a}{h-a}\right)^{\mathrm{Z}} \tag{23}$$

Here z is the distance from the center of the grid point nearest to the bed (Olsen, 2003) and Z is the Rouse number given by $Z = w_s/(\kappa U_*)$.

The excess sediment slides down when the bed slope exceeds the angle of repose (φ). This process is accounted for using a sand slide algorithm (Burkow and Griebel, 2016) implemented in the morphological model. A correction of -2° is applied when the bed slope exceeds the angle of repose φ (Roulund et al., 2005).

The shape of scour holes are seen to be asymmetrical (Sumer et al., 2002a). As the downhill bed slope is expected to be larger than the uphill bed slope, the angle of repose for the downhill slope is assumed to be $\varphi = 45°$, and for the uphill bed slope, $\varphi = 35°$ (Lysne, 1969b; Bihs, 2011; Ahmad et al., 2018b). The change in bed elevation is calculated with Exner's formula (see Eq. 24). The formula ensures the conservation of the sediment mass, where the spatial variation in the bed load is conserved with the temporal change in the vertical bed elevation. The morphological evolution occurs as a nonlinear propagation of the bed-level deformation in the direction of the sediment transport. The transient change in bed level is defined as follows:

$$\frac{\partial z_b}{\partial t} + \frac{1}{(1-n)} \left[\frac{\partial q_{B,x}}{\partial x} + \frac{\partial q_{B,y}}{\partial y} \right] + E - D = 0 \tag{24}$$

Here, z is the bed-level, $q_{B,x}$ is the bed load in the x-direction, $q_{B,y}$ is the bed load in y-direction, $n = 0.40$ is the sediment porosity. The term $(E - D)$ defines the net flux of sediment across the interface between the bed load and suspended load and is calculated as suggested by Wu et al. (2000). The changes in bed elevation are modelled with the level set method, which is an implicit representation of the sediment bed as the zero level set. The driving factor is $F = \partial z_b/\partial t$ which moves the interface in the vertical direction to represent the erosion and the deposition.

2.4 Numerical schemes and solver

The model approximates spatial derivatives using higher-order finite difference methods. A uniform Cartesian grid is used throughout the domain where dx=dy=dz. The convective terms of the RANS equations are discretized with the fifth-order accurate conservative Weighted Essential Non-Oscillatory (WENO) scheme (Jiang and Shu, 1996). The convective terms of the turbulence model and the level set function are discretized with the Hamilton-Jacobi formulation of the WENO scheme (Jiang and Peng, 2000). A third-order TVD Runge-Kutta time scheme (Shu and Osher, 1988) is used for time treatment of the RANS equations and the level set function. The hydrodynamic time step for the transient flow field is determined using adaptive time stepping in order to maintain optimal efficiency and stability and is obtained based on the Courant-Friedrichs-Lewy (CFL) number. The pressure is treated with the projection method (Chorin, 1968). The BiCGStab (van der Vorst, 1992) solver from the high-performance solver package HYPRE with the semi-coarsening multi-grid preconditioner PFMG (Ashby and Falgout, 1996) is implemented to solve the Poisson equation for the pressure. The complex solid boundary of the structure and bed are defined with an immersed boundary method with the local directional ghost cell approach (Berthelsen and Faltinsen, 2008).

3 Numerical setup

The first setup used for the validation of the numerical model is based on the benchmark experimental investigation by Sumer et al. (1992). The experiments were carried out in a 28 m long and 4 m wide and 1 m deep wave flume. The investigations involved several tests with different pile diameters and wave conditions. The simulations are performed in an NWT of length 8.8 m and width 2.0 m with a large pile of diameter $D = 0.20$ m. The pile is placed at the centre of the NWT. For all simulations, the water depth is $h = 0.40$ m. The bottom of the NWT (z = -0.30 m) is filled with sand of the median grain size $d_{50} = 0.18$ mm. The density of the sediment is $\rho_s = 2700$ kg/m^3. The critical shields parameter which defines the initiation of motion of sediment particles is considered to be $\theta_c = 0.05$. The simulations are performed for five different KC numbers which define the orbital motion of the water particles relative to the width of the pile (Sumer and Fredsøe, 1997). The experiments conducted in the wave flume by Sumer et al. (1992) did not investigate the scour under a steady current for the large vertical pile and therefore the experiment by Link (2006) is used. The diameter of the cylinder is $D = 0.20$ m. The still water depth is $h = 0.30$ m. The steady current velocity is $u = 0.30$ m/s. The median grain size is $d_{50} = 0.97$ mm. The other properties are the same as used in the previous simulations. The details of the simulations performed are listed in Table 1.

No.	dx (m)	CFL	T (s)	u_m (m/s)	D (cm)	λ (m)	H (m)	kH	KC	Duration (s)	Measured S/D	Num S/D
Grid size convergence study in a empty NWT												
$A1$	0.04	0.25	4.5	0.53	-	8.8	0.21	0.15	-	225	-	-
$A2$	0.03	0.25	4.5	0.53	-	8.8	0.21	0.15	-	225	-	-
$A3$	0.02	0.25	4.5	0.53	-	8.8	0.21	0.15	-	225	-	-
$A4$	0.01	0.25	4.5	0.53	-	8.8	0.21	0.15	-	225	-	-
Time step size convergence study in an empty NWT												
$B1$	0.01	0.40	4.5	0.53	-	8.8	0.21	0.15	-	225	-	-
$B2$	0.01	0.30	4.5	0.53	-	8.8	0.21	0.15	-	225	-	-
$B3$	0.01	0.20	4.5	0.53	-	8.8	0.21	0.15	-	225	-	-
$B4$	0.01	0.10	4.5	0.53	-	8.8	0.21	0.15	-	225	-	-
Local scour around pile under wave (Sumer et al., 1992)												
$C1$	0.01	0.10	4.5	0.30	0.20	8.8	0.12	0.08	6.81	3600	0.032	-0.04
$C2$	0.01	0.10	4.5	0.32	0.20	8.8	0.13	0.09	7.41	3600	0.055	-0.06
$C3$	0.01	0.10	4.5	0.39	0.20	8.8	0.16	0.10	8.89	3600	0.057	-0.08
$C4$	0.01	0.10	4.5	0.46	0.20	8.8	0.19	0.13	10.66	3600	0.085	-0.10
$C5$	0.01	0.10	4.5	0.53	0.20	8.8	0.21	0.15	12.11	3600	0.110	-0.14
Scour under a steady current (Link, 2006)												
$D1$	0.01	0.10	-	0.30	0.20	-	-	-	∞	75600	0.70	-0.68
Local scour around a jacket (Bolle et al., 2012)												
$E1$	0.20	0.10	23.0	-	2.0	394.0	4.5	0.011	7.0	3600	0.65	-0.80
$E2$	0.20	0.10	-	0.60	2.0	-	-	-	∞	3600	0.90	-0.70

Table 1: List of simulations run for scour around the pile and jacket structure.

4 Model validation

4.1 Grid and time step size convergence study

At first, the grid size and time step convergence tests are performed in an NWT without structure. The purpose of the tests is to determine the minimum grid size required to maintain the quality of the generated waves during propagation along the wave flume as shown in Figs.

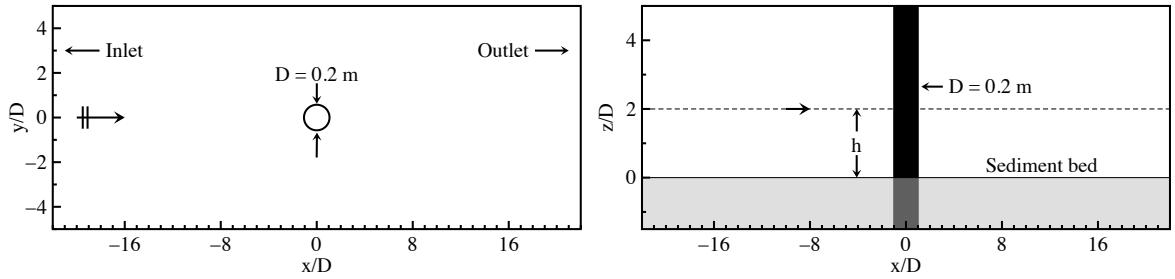

(a) Top view (b) Side view

Figure 1: The numerical setup used for the validation. Source of experimental data: Sumer et al. (1992)

1(a-b). Fifth-order Cnoidal waves are chosen based on the incident wave characteristics. One wave gauge is located at the center of the tank, $x/D = 0$, where the pile is to be fixed. The numerical tests are run by considering the steepest wave of steepness $kH = 0.15$, where $k = 2\pi/\lambda$ is the wave number, $\lambda = 8.8$ m is the wavelength, and $H = 0.25$ m is wave height analysed in the experiment (Sumer et al., 1992). Four different grid sizes, $dx = dy = dz =$ 0.04 m, 0.03 m, 0.02 m, and 0.01 m, are tested. For all grid sizes, the CFL number is kept at 0.25. The results show the accuracy of the simulated waves through comparison with wave theory. Figs. 2(a-d) show the simulated wave surface elevations for different grid sizes. It is found that the wave accuracy increases with a decrease in grid size dx. The quality of the wave is considered to be satisfactory for a grid size $dx = 0.01$ m and CFL = 0.25.

In order to further improve the quality of the propagated waves, tests are performed for the time step size. The calculation of the transient flow hydrodynamics is based on an adaptive time stepping where the time step size is attributed to the Courant-Friedrichs-Lewy (CFL) number. Therefore, instead of testing a fixed time step size, different CFL numbers, i.e., CFL = 0.40, 0.30, 0.20 and 0.10 are tested. The grid size of $dx = 0.01$ m is maintained for all following simulations. Figs. 3(a-d) shows a comparison between the simulated free surface elevations and the wave theory for different CFL numbers. The wave quality is observed to increase with a decrease in CFL numbers. It can be seen that the wave crests and wave troughs are slightly overestimated for CFL = 0.10. This is due to the propagation of relatively a high ($H = 0.21$ m) and steep wave ($kH = 0.15$) in the shallow water. The quality of the wave is considered to be reasonably good for a grid size $dx = 0.01$ m and CFL = 0.10 and the solution is considered to be converged. However, the quality of a wave with a low wave steepness $kH = 0.08$, can be found in Ahmad et al. (2018*b*). Results show a good match of the propagating waves with the wave theory for $dx = 0.01$ m and CFL = 0.10.

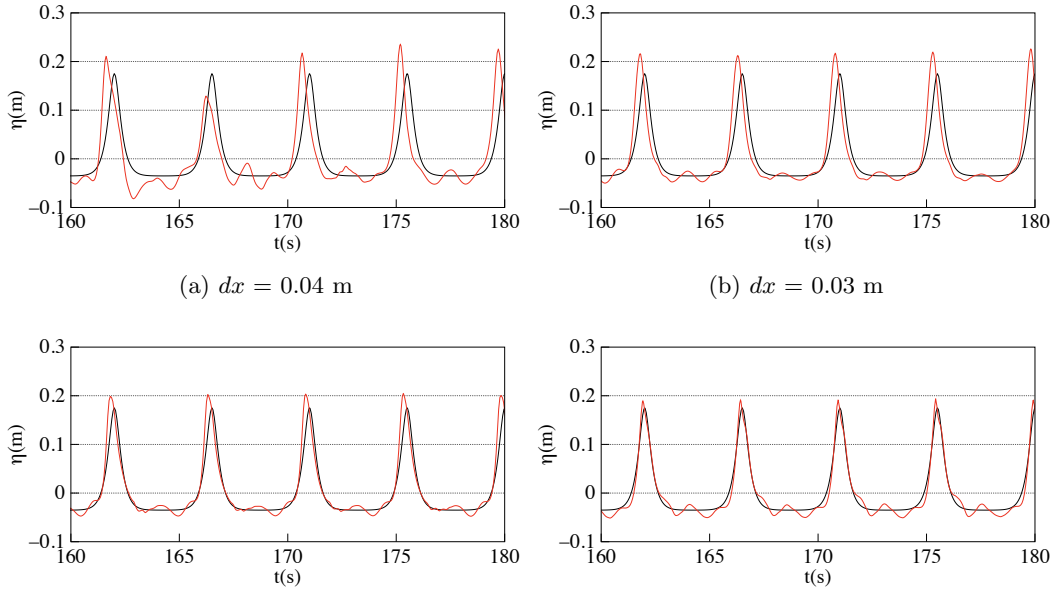

(a) dx = 0.04 m (b) dx = 0.03 m

(c) dx = 0.02 m (d) dx = 0.01 m

Figure 2: Grid size convergence study, cases A1-A4. A comparison between the simulated free surface elevations and the wave theory at location x/D = 0. The wave steepness is H/L = 0.024, the wave period is T = 4.5 s, and CFL = 0.25.

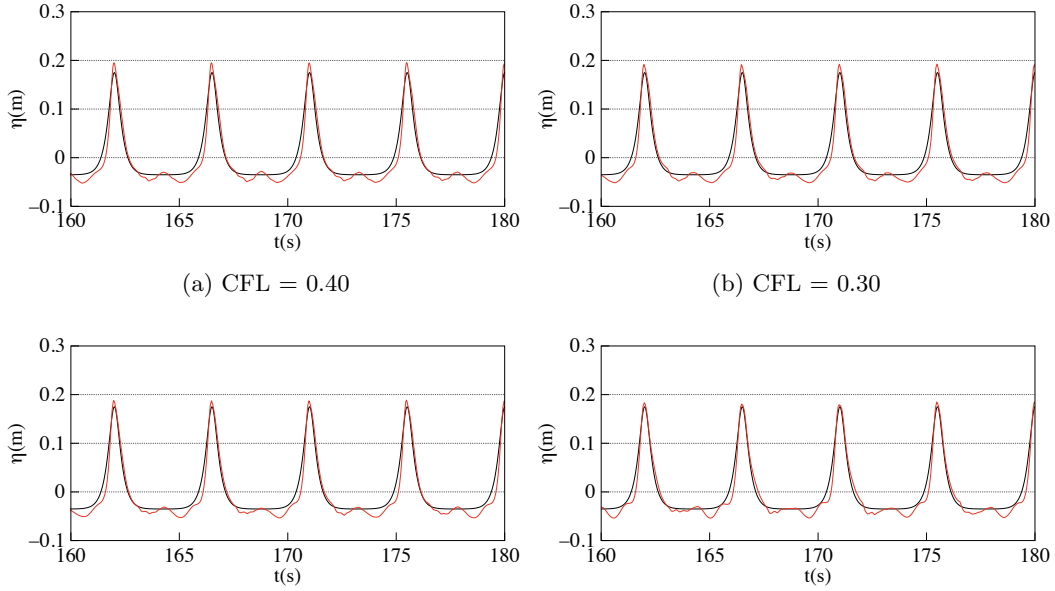

(a) CFL = 0.40 (b) CFL = 0.30

(c) CFL = 0.20 (d) CFL = 0.10

Figure 3: Time convergence study, cases B1-B4. A comparison between the simulated free surface elevations and the wave theory at location x/D = 0. The wave steepness is H/L = 0.024, the wave period is T = 4.5 s, and dx = 0.01 m.

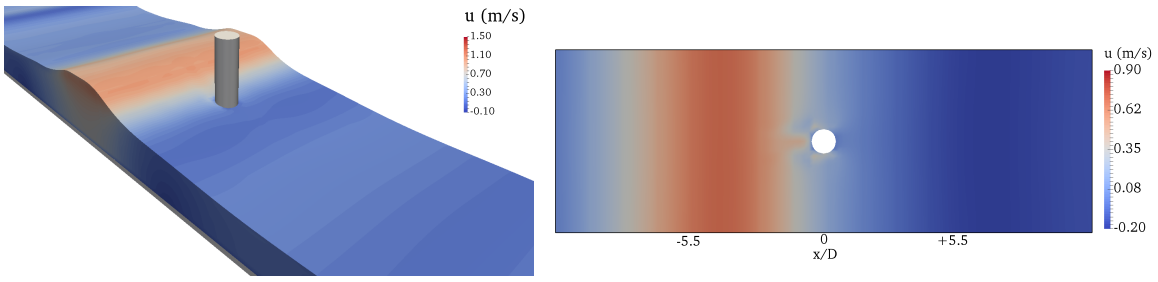

(a) Free surface velocity, $t/T = 0.40$ (b) XY plane, Z/D = 1.0

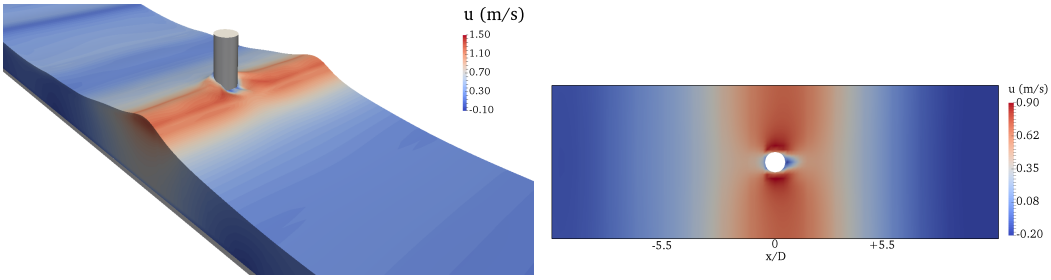

(c) Free surface velocity, $t/T = 0.50$ (d) XY plane, Z/D = 1.0

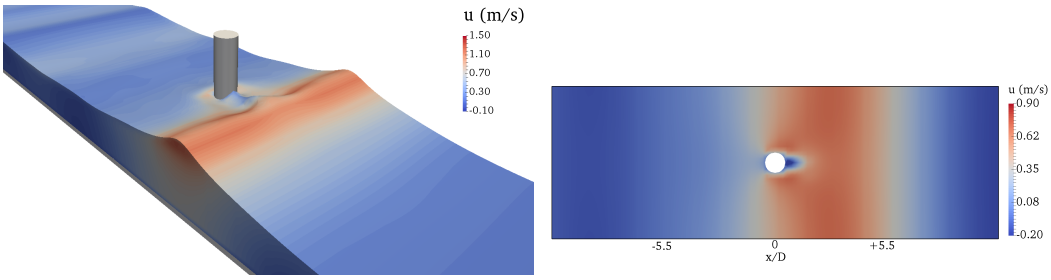

(e) Free surface velocity, $t/T = 0.55$ (f) XY plane, Z/D = 1.0

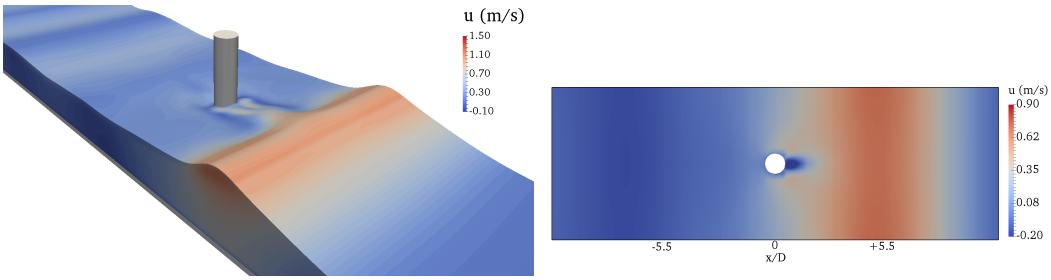

(g) Free surface velocity, $t/T = 0.60$ (h) XY plane, Z/D = 1.0

Figure 4: Simulated free surface around the pile exposed to wave and change in hydrodynamics $Z/D = 1.0$ aboved the bed. The incident wave conditions are: the wave height $H = 0.21$ m, the wave period $T = 4.5$ s, KC $= u_m T/D = 12$. Source of experimental data: Sumer et al. (1992)

4.2 Scour around the pile exposed to waves

This section describes the simulation of the local scouring process under the presence of a dynamic free surface. The scour results for the case with KC = 12 are discussed in detail. The results of the remaining tests show a similar temporal variation of the maximum scour depth and scour hole pattern after $t_s = 60$ minutes and therefore the results are presented only for the change in scour depth (S/D) against the KC number.

The simulations are run for different KC values using the partial decoupling approach. This implies that the bed evolves with the change in hydrodynamics at each time step. However, instead of using a common time step size for the hydrodynamic and morphological models, an increased time step for the morphological model is employed. The increment of the morphological time step corresponding to the hydrodynamic time step is defined as the decoupling factor $DF = \Delta t_s/\Delta t$. Here, Δt_s is the time step for the morphological model and Δt is the time step for the hydrodynamic model. The decoupling factor DF = 1.0 refers to a fully coupled hydrodynamic and morphological models. The decoupling factor for the scour around monopile simulations is $DF = 6.6$ as in Ahmad et al. (2018*b*). The partial decoupling approach is implemented as: The simulated flow is coupled with the bed load and suspended load which is linked to the Exner's equation at each hydrodynamic time step. The bed evolution is calculated using the morphological time step t_s and represented with the level set function $\phi(\vec{x}, t)$. The level set function changes the signed distance property with the bed evolution. Hence, the function is reinitialised at each hydrodynamic time step. The process is repeated with the change in hydrodynamics until an equilibrium scour state is maintained. This approach helps in reducing the computational cost significantly.

Fig. 4(a) shows the free surface velocity of the incoming wave. The maximum wave orbital velocity is $u_m = 0.53$ m/s, the incident wave height is $H = 0.21$ m, the wave period is $T = 4.5$ s and the Keulegan-Carpenter number is calculated to be KC = $u_m T/D = 12$. The flow around the pile depicts a stage where the pile is exposed to the wave crest action. Fig. 4(b) shows a zoomed-in view of the near-bed velocity contour in the vicinity of the pile. The plane is located at $z/D = 1.0$ above the bed. Figs. 4(c-h) are the sequence of the wave incident on the pile. The maximum velocities beside the pile are seen to be $u = 0.90$ m/s. However, the downstream side of the pile shows relatively lower velocities u = -0.20 m/s. Thus, an increase in the velocities at the sides of the pile compared to the maximum incident velocities contributes to a higher bed shear stress around the pile and results in higher sediment transport from this region. The lower velocities at the downstream side develop a relatively lower bed shear stress and consequently lower sediment transport.

Figs. 5(a-d) show the sequence of the scour development around the pile. The maximum scour around the pile is found to be S/D = -0.14 and the deposition at the downstream side are $S/D = 0.12$. The magnitude of the deposition is comparable to the scour depth. This is attributed to the wave-induced local scour where sediments are not transported away from the region as in the case of a steady current. Fig. 5(e) shows the temporal variation of the local scouring process. It is seen that the major part of the maximum scour takes place within the first 20 minutes. The fluctuations in the scour depth pattern represent the scouring and refilling with the wave crests and troughs. Fig. 5(f) shows the change in maximum scour depth S/D around the pile depending on the KC number. It is found that S/D increases with the KC number. The scour depth is found to be four times higher at KC = 12 compared to KC = 6.81 due to the higher wave activity around the pile. The results show a good agreement

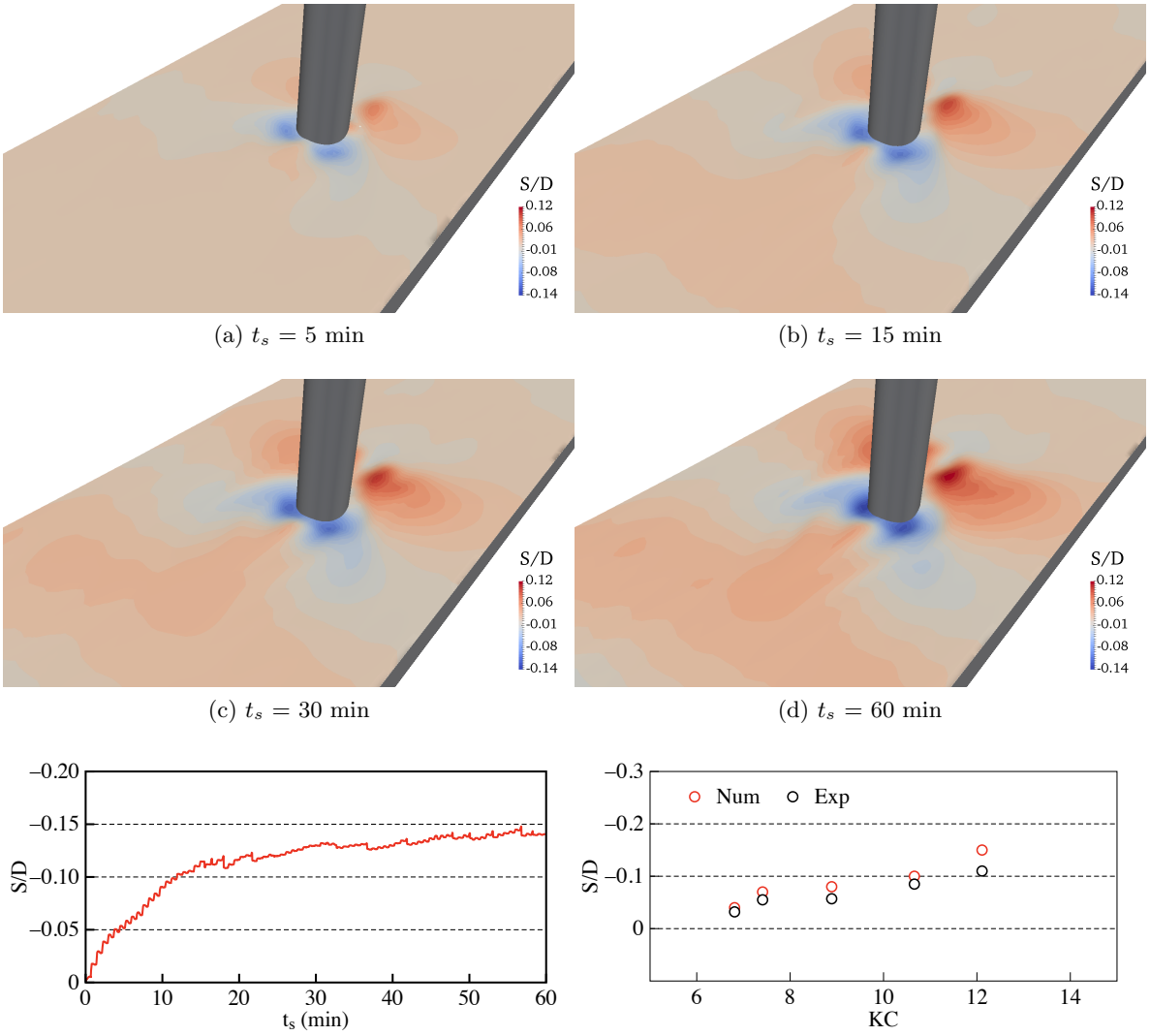

(a) t_s = 5 min

(b) t_s = 15 min

(c) t_s = 30 min

(d) t_s = 60 min

(e) Temporal variation of the wave-induced scour

(f) Change in scour depth (S/D) against KC

Figure 5: Simulated scour around the pile exposed to wave. Experiment data: Sumer et al. (1992)

with the experimental observations (Sumer et al., 1992), which confirms the accuracy of the model regarding the simulation of scour around a vertical pile exposed to wave action.

4.3 Scour around the pile exposed to a steady current

Figs. 6(a-b) present the scour around the pile under a steady current. In this case, the incident flow velocity is u = 0.30 m/s. The velocity on either side of the pile is seen to be u = 0.35 m/s due to the flow contraction. However, the velocity in the shadow region is seen to be lower with the velocity u = -0.10 m/s. The converging streamlines in the shadow region indicate the presence of the wake vortices which is considered to be the main cause of scour at the downstream side of the pile (Sumer and Fredsøe, 1990).

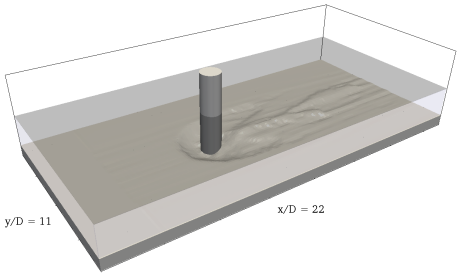

(a) Simulated scour with free surface profile

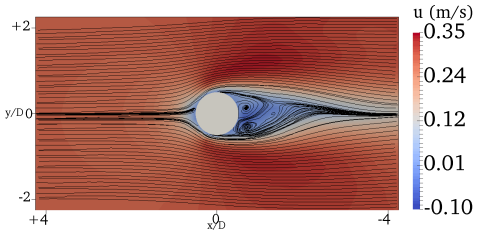

(b) Velocity around the pile. XY plan, Z/D = 1.0

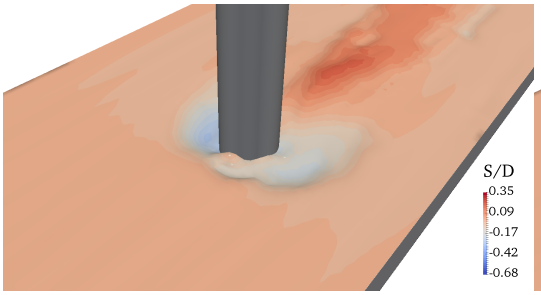

(c) Simulated scour at t_s = 5 min

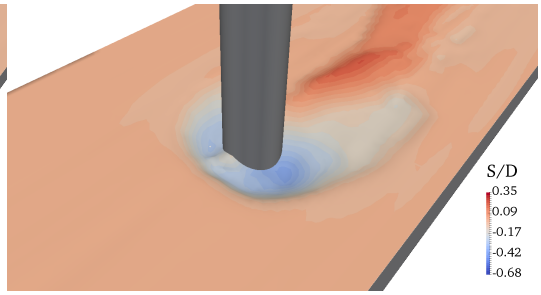

(d) Simulated scour at t_s = 5 h

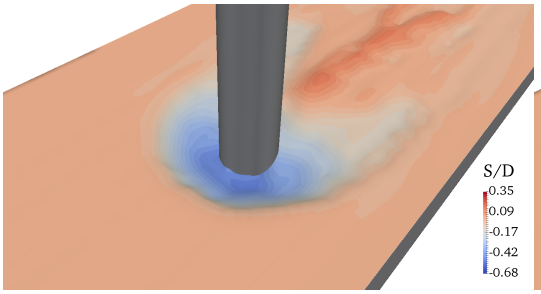

(e) Simulated scour at t_s = 10 h

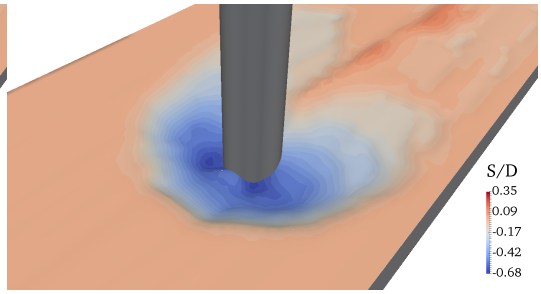

(f) Simulated scour at t_s = 20 h

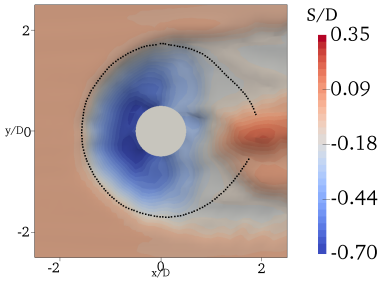

(g) Simulated maximum scour depth, top view

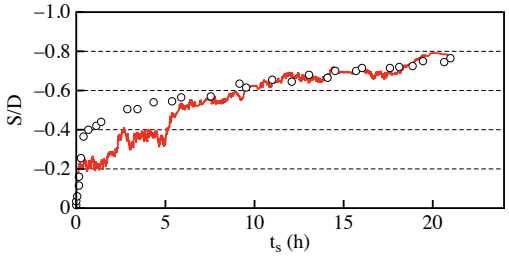

(h) Temporal variation of maximum scour depth

Figure 6: Simulated hydrodynamics and resulting scour around the pile exposed to a steady current. The incident flow velocity is u = 0.30 m/s. The black dots and circles in figs. 6(g-h) are the Experiment data from Link (2006).

Figs. 6(c-f) depict the development of the scour depth at different time intervals. It is

found that the scouring process is initiated from the sides of the pile and propagates around the pile with time. The scour at the sides and front of the pile is seen higher compared to the scour at the downstream side. This indicates that a high flow activity on the upstream side of the pile and the higher velocity beside the pile; leads to the formation of horseshoe vortices at the upstream side which govern the maximum scour (Chiew and Melville, 1987; Sumer et al., 2002*b*; Baykal et al., 2015). Fig. 6(g) shows the final stage of the scour around the pile after 20 hours. The scour depth and extent is presented in top view. The maximum scour depth around the pile is seen to be S/D = -0.70. The scour around the pile depicts almost a circular profile with scour extents $(x/D, y/D)$ range -1.8 to 1.8. The scour profile shows a satisfactory match with the experiment (Link, 2006) as shown with the black dots. The scour at the upstream side of the pile is in good agreement with the experiment. However, the scour depth at the downstream side of the pile is slightly underpredicted and is followed by the deposition.

Fig. 6(h) shows the temporal variation of the process for simulation. It is seen that almost half of the maximum scour, i.e., S/D = -0.35 is achieved within a few minutes. Once the scour hole is formed, the maximum scour depth stagnates as the sediment slides into the scour hole from the outer regions. This results in an increase of the scour hole width. When the scour hole becomes wide enough, there is a decrease in the flow velocities and bed shear stress in the scour hole. Consequently, the scour depth rate decreases with the scour hole development. It is found that scour depth during the initial and final stage of the scouring process shows a good match. The intermediate scour depth is relatively lower compared to the experiment. This is more likely due to the mesh resolution around the pile. In addition, the boundary layer and the individual vortex shedding mechanism is not resolved with this approach. These processes represent important flow features close to the solid boundary and consequently the local scour. The restriction on the complete representation of these processes can contribute to the differences seen between the numerical results and the measurements.

Eventually, the simulated scour topography, the maximum scour depth and the temporal variation of the scouring process depict an adequate agreement with the experiment (Link, 2006). The numerical results demonstrate the ability of the model to simulate the local scour around a pile under waves and a steady current conditions.

5 Scour around a jacket structure

The validated numerical model for the scour around a monopile under waves and current is used to simulate the scour around a jacket structure. The wave conditions and sediment properties are taken from the C-power wind farm Thornton bank, which is located 30 km from the Belgian coast (Bolle et al., 2012). The jacket is comprised of four vertical piles connected with the diagonal bracings. The diameter of the vertical piles is D = 2.0 m and the gap between the individual foundations is G/D = 10. The still water depth on the site ranges between 12 m to 30 m. In the present study, the highest still water depth of h = 30.0 m is considered. The bed material is sand of the median grain size d_{50} = 0.30 mm and the density of the sediment is ρ_s = 2700 kg/m^3. The angle of repose for the downhill slope is $\varphi = 45^\circ$, and for the uphill bed slope, $\varphi = 35^\circ$ following Lysne (1969*a*) and Bihs and Olsen (2011), where the direction of flow results in different angles of repose. The critical shields parameter for the bed material is θ_c = 0.05 (Bolle et al., 2010). According to the

hydrodynamic measurements from the site, the waves of wave height range 3.5 - 4.5 m were observed under storm conditions in January 2012 and the average scour depth is seen to be S/D = -0.85 to -1.35, which is considered to be a developed scour depth as per DNV GL guidelines (DNV, 2014). This case is simulated by considering a typical condition of a storm of wave height H = 4.5 m, still water depth h = 30, wave period T = 23.0 s, and KC = $2\pi a/D$ = 7.0. The morphological calculation of 60 minutes is obtained with DF = 6.8. The simulation is run until the morphological calculations of 60 minutes is achieved. For KC = ∞, the jacket platform is exposed to a steady current flow velocity with u = 0.60 m/s. The details of the prototype are listed in Table 1.

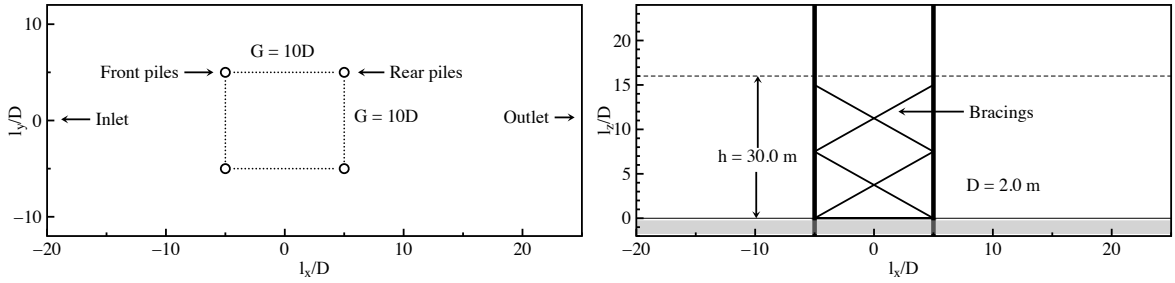

(a) Top view (b) Side view

Figure 7: Numerical setup used for local jacket scour under waves and current. Still water depth = 30.0 m, gap between the piles is G/D = 10, Diameter of the piles is D = 2.0 m. Source of field data: Bolle et al. (2012). Figure is not drawn to scale.

5.1 Scour around a jacket structure exposed to waves

In this section, results of the scour around the jacket exposed to waves are discussed. The simulation is run for t = 60 minutes. The results describe the flow velocities at the free surface, changes in the velocities close to the bed and the resulting local scour. The diameter of an individual pile of the jacket structure is D = 2.0 m and the gap between the piles is $G = 10D$. It requires a minimum $l_x = 22D + G = 32D$ = 64.0 m long, $l_y = 10D + G = 20D$ = 40.0 m wide, and l_z = h + minimum cover above the still water depth = 30 m + 10 m = 40 m high NWT for the wave generations and propagation as shown in Figs. 7(a-b). The size of the NWT is based on truncated length of the NWT tank required for wave propagation in the NWT (Ahmad et al., 2018*b*). The width is assumed to be sufficiently wide to maintain an undisturbed flow around the jacket platform (Breuer et al., 2000). The numerical modelling of such large numerical NWT needs large computational resources. Therefore, a coarse grid size of dx = 0.20 is used to run the simulations for scour around the jacket platform. The selection of the grid size (dx) is based on the number grid cells around the pile i.e., D/dx = 10. This criterion has already been tested for scour around the piles in a side-by-side arrangement by Ahmad et al. (2018*b*). To ensure the quality of the wave propagation, the wave is generated and propagated in the NWT without a jacket platform. Fig. 8 shows the computed free surface elevations. It can be seen that the simulated wave elevations show a good match with the wave theory. This confirms the accuracy of the wave generation and the propagation in the large NWT with dx = 0.20 m. Hence, the model is implemented to simulate the local

scour by introducing a jacket platform in the NWT in the following simulations. The focus is on the change in wave hydrodynamics and the resulting scour around a jacket platform exposed to wave and steady current.

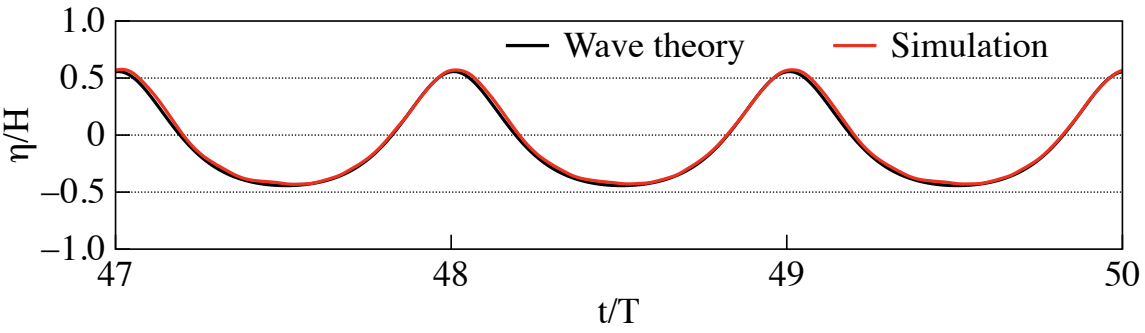

Figure 8: A comparison between the simulated free surface elevations and the wave theory for $dx = 0.10$ m. The wave is generated in an empty wave tank. The wave gauge location x/D = 0; still water depth = 30.0 m, incident wave height $H = 4.5$ m, the wave theory: fifth-order Cnoidal waves.

Fig. 9(a) shows the free surface when the wave crest is incident on the jacket. The velocities around the vertical piles vary between $u = 4.0$ to 5.0 m/s. The velocities in the shadow region of the vertical piles and outside the jacket are seen to range from $u = 0$ to -2.0 m/s. Fig. 9(b) shows the free surface velocity under wave trough. The free surface elevation is lowered to 27.5 m and velocities around the jacket vary between -1.6 and 1.0 m/s.

Fig. 9(c) shows the velocity contour on a plane 0.10 m above the bed when the wave crest is incident on the jacket. The velocities outside the jacket range between 1.0 and 1.5 m/s. However, the velocities around the vertical piles and under the lateral bracings of the jacket seem to vary between -1.5 to 3.5 m/s which are almost two times higher compared to the velocities in the outside region of the jacket. The increase in the velocities around the jacket is due to the flow contraction around the vertical piles and the formation of a flow jet between the lateral bracing and the bed. The velocities inside the jacket seem almost similar to the velocities seen outside the jacket. Fig. 9(d) shows the velocities during wave trough. It is seen that the flow hydrodynamics are similar to the ones seen during wave crest action but in the opposite direction. The velocities around the vertical piles and below the bracings range from 1.0 to -1.5 m/s. The velocities at on the downstream side of piles are higher compared to the upstream side of the jacket.

Figs. 9(e) shows the scour when the waves are incident on the jacket. It is seen that the higher velocities around the vertical piles and the bracing leads to a higher scour depth around the jacket. However, the inside region of the jacket structure is subjected to relatively lower velocities; consequently, the eroded sediment from the front piles are deposited inside the jacket.

Fig. 9(f) shows scour around the jacket structure during the wave trough. A large scour at the rear side of the jacket is evident. This is due to the high velocities seen around the vertical piles and below the bracings during the wave trough. It can be seen that deposition inside the jacket is further increased. Overall, the higher velocities around the vertical piles and under the lateral bracings indicate flow contractions and formations of jet flow. This

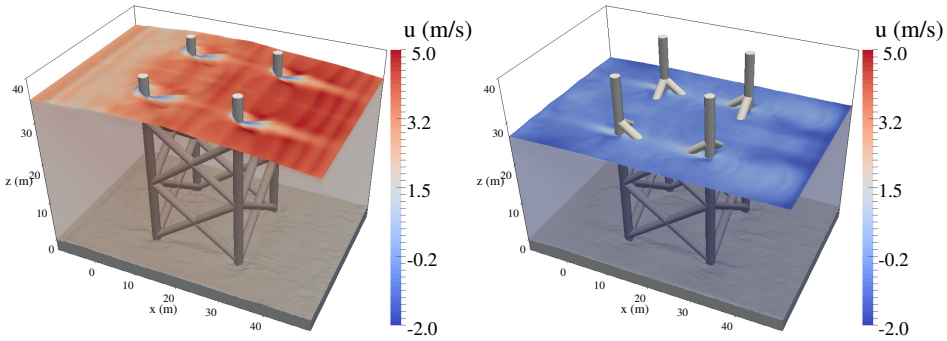

(a) Free surface velocity during wave crest (b) Free surface velocity during wave trough

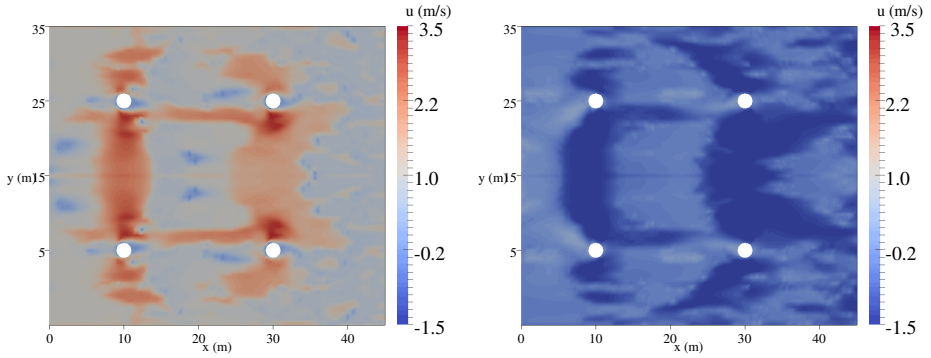

(c) Velocities close to the bed during wave crest (d) Velocities close to the bed during wave trough

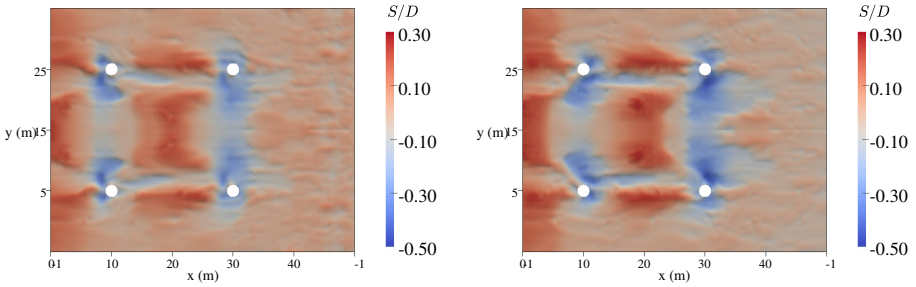

(e) Scour developed during the wave crest (f) Scour developed during the wave trough

Figure 9: Simulated flow field and scour around the jacket exposed to waves after $t_s = 5$ minutes. Incident wave conditions are: incident wave height $H = 4.5$ m, still water depth is $h = 30.0$ m, wave period is 23.0 s, and pile diameter is 2.0 m. The velocities close to the bed presented in Figs. 7(c-d)refers to a xy-plane 0.10 m above the bed.

change in flow hydrodynamics leads to the local scour around at the vertical piles and lateral bracings, and the deposition inside the jacket.

Figs. 10(a-d) demonstrate the scour evolution at $t_s = 15$, 30, 45 and 60 minutes. It

is seen that the scour is initiated at the vertical cylinders of the jacket and is increasing over time. The magnitude of maximum scour depth is S/D = -0.80 and the deposition is S/D = 0.50. The scour depth at the front piles of the jacket is lower compared to the rear piles. This is due to the continuous process of intensive scouring at the front piles during wave crest and re-filling of deposited sediment during the wave trough. However, at the rear piles of the jacket, the sediments removed during the wave crest are transported away in the direction of the wave propagation; therefore, there is almost no re-filling occurs during the wave trough. Consequently, a high scour depth can be observed at the rear piles of the jacket. The simulated scour pattern around the jacket is well supported by the experiments conducted for scour around a tripod structure by Stahlmann (2013), where a higher scour at the rear side of the tripod is measured. Fig. 10(e) shows the temporal variation of the

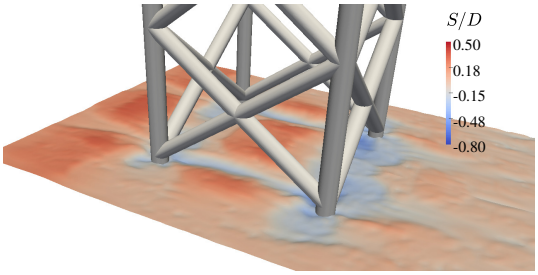

(a) Simulated wave-induced scour at t_s= 15 min

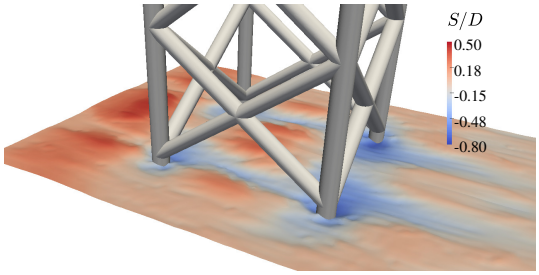

(b) Simulated wave-induced scour at t_s= 30 min

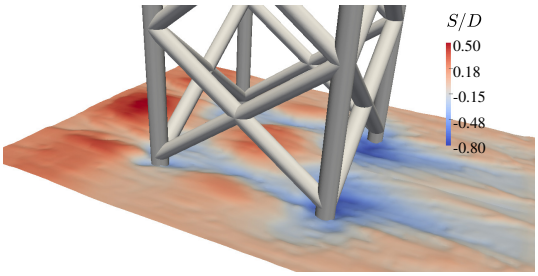

(c) Simulated wave-induced scour at t_s= 45 min

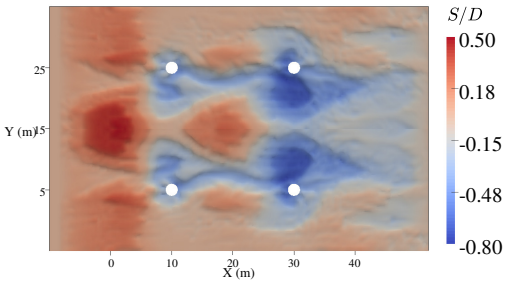

(d) Simulated wave-induced scour at t_s= 60 min

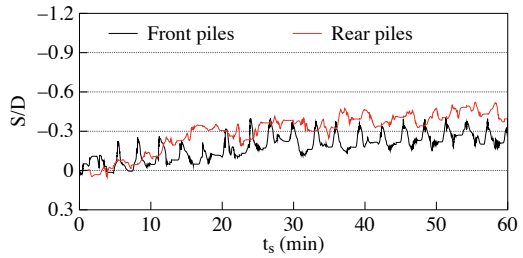

(e) Maximum wave-induced scour at front and rear piles

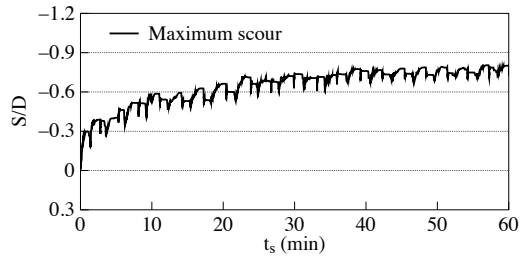

(f) Maximum wave-induced scour around the jacket

Figure 10: Time development of the scouring process around the jacket structure. (a-d) depicts scour 3D and 2D top view of the scour profile; (e) the black line represents scour around the front piles and the red line depicts scour around the rear piles of the jacket structure; and (f) the maximum scour around the jacket structure is represented with the thick black line.

maximum scour at the front and rear piles. The spikes in the graph represent the change in the maximum scour depth with wave crests and troughs. It is seen that the interaction of the wave crest with the jacket leads to a high scour depth at the front pile. The scour depth during a wave peak is almost S/D = -0.30. However, during the wave trough, a significantly higher backfilling of the scour hole is evident. This results in a decrease in the scour depth around the vertical piles. The maximum scour depth at the front pile after 60 minutes is seen to be S/D = -0.40. At the rear pile, the scour depth seems to be increasing with a faster rate and without a significant backfilling. This leads to a deeper scour hole at the rear piles. The maximum scour depth at the front pile after 60 minutes is S/D = -0.50. Fig. 10(f) shows the temporal variation of the maximum scour depth around the jacket. It can be seen that the maximum scour depth grows rapidly in the beginning and slows down as it approaches an equilibrium state after t_s = 60 minutes. The magnitude of the maximum scour depth is S/D = -0.80 which is under the bracing attached with rear piles of the jacket. The simulated scour depth S/D agrees with field observations (Bolle et al., 2012) of average of the maximum scour depths S/D = 0.85 - 1.35 observed after one storm.

5.2 Scour around a jacket structure exposed to a steady current

As the scour depth increases with the KC number, another simulation is run for the scour around the jacket structure exposed to a steady current which corresponds to KC = ∞. The incident flow velocity is u = 0.60 m/s which represents a typical flow condition in the field (Bolle et al., 2012). The simulation is run for t_s = 60 minutes. The results for the scour under a steady current reveal the complex hydrodynamics, the maximum scour depth and the temporal variation of the scouring process around the jacket structure. Figs. 11(a-b) show the free surface flow around the jacket and velocities on a plane 0.10 m above the bed. The velocities around the jacket range from 0.60 to 1.0 m/s. An increase in the velocities on either sides of the piles and below the lateral bracings due to flow contraction and the formation of jet flow can be noticed. The region on the downstream side of the piles shows a converging flow with the velocities in the range of u = 0 to -0.20 m/s. The results clearly show higher velocities around the vertical piles, this results in higher scour around the vertical piles at the front and rear piles. However no significant scour is observed below the bracings as shown in Figs. 11(c-f). The magnitude of maximum scour depth is seen to be S/D = -0.70. In comparison to the deposition observed in the case of the oscillatory fluid motion of the waves, the eroded sediments are washed away by the steady flow and a reduced deposition is observed in the shadow region of piles at the jacket.

Fig. 12(a) shows the temporal variation of the maximum scour observed at the front and rear piles. As the front piles are directly exposed to the steady flow, it leads to a higher scour. The scour depth at the front piles is seen to be S/D = -0.70. The scour depth at the rear piles is seen to be S/D = -0.50. There is insignificant re-filling of the scour hole, as seen in case of waves. The scour at both the front and rear piles reveal a rapid and continuous scour growth over time. The maximum scour depth around the jacket is seen to be S/D = -0.70 which is at front piles. the results demonstrate that an equilibrium scour depth is not yet achieved.

Fig. 12(b) shows the variation of the maximum scour depth S/D with increasing KC number. The simulated scour depth for all scenarios is compared with Sumer et al. (1992) formula (Sumer et al., 1992). The result shows that the scour depth calculated for a monopile

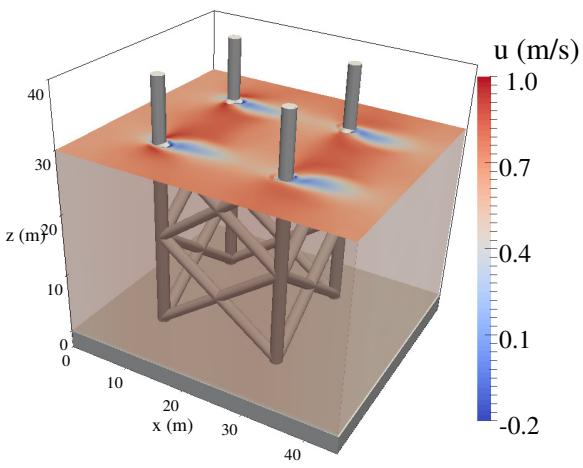

(a) Free surface velocity profile under a steady current

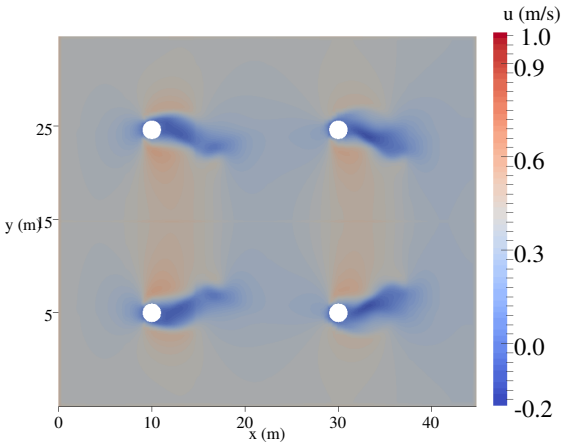

(b) Velocities 0.10 above the bed

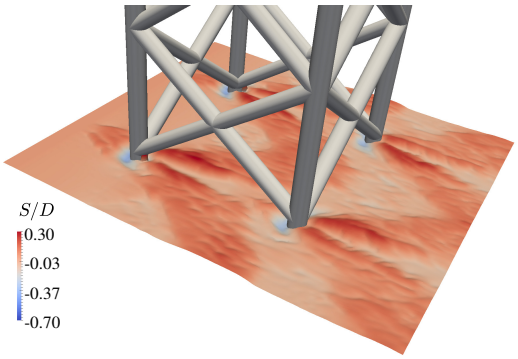

(c) Current-induced scour at t_s= 15 min

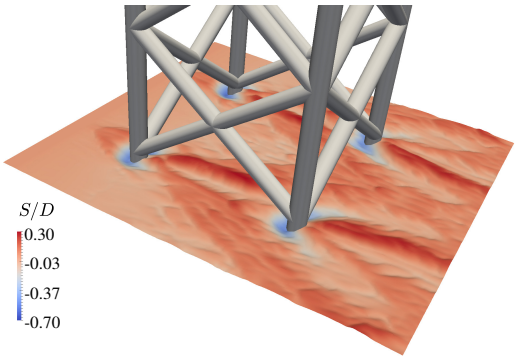

(d) Current-induced scour at t_s= 30 min

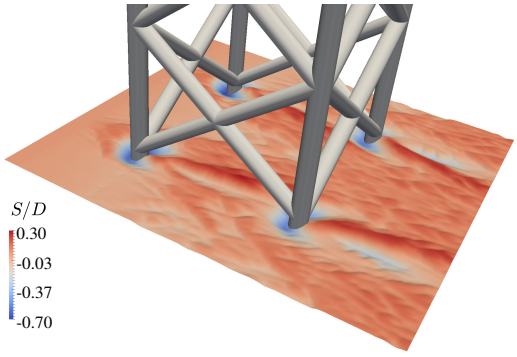

(e) Current-induced scour at t_s= 45 min

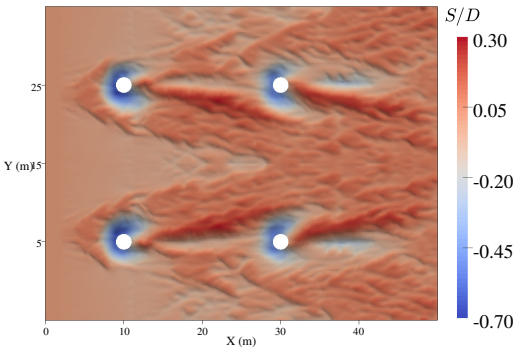

(f) Current-induced scour at t_s= 60 min

Figure 11: Simulated flow field and scour around the jacket exposed to a steady current. Incident wave conditions are: inflow velocity = 0.60 m/s, still water depth is h = 30.0 m, and pile diameter is D = 2.0 m.

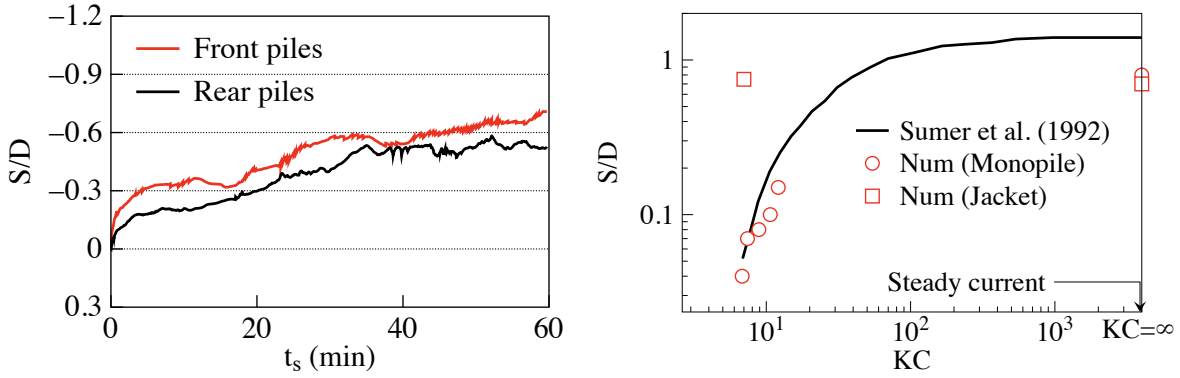

(a) Scour at the front and rear piles of jacket

(b) Variation of S/D with KC for a monopile.

Figure 12: Development of the scouring process around the jacket piles under a steady current and a comparison of simulated scour depth using formula developed for scour around a monopile.

shows a close match. However, for a jacket the maximum scour simulated around the jacket for KC =7.0 is almost 10 times higher compared to the scour depth for a monopile. The observation suggests a careful consideration for the estimation of maximum scour depth around jacket structure using the empirical formulae developed for a monopile.

6 Conclusions

In this paper, numerical modelling of local scour with free surface capturing around a jacket structure is presented. The open-source CFD model REEF3D is used to simulate the flow hydrodynamics by solving the RANS-equations with the k-ω turbulence model. The free surface is captured with the level set method. The simulated flow hydrodynamics are coupled with the sediment transport algorithms to simulate the local scour. The sediment transport algorithms account for the effect of the sloping bed for the calculation of the critical bed shear stress. In order to obtain a more realistic prediction of the scour hole, a sand-slide algorithm is incorporated to correct the bed slope when it exceeds the angle of repose. The changes in the bed level are based on Exner's formula. A series of simulations are conducted for local scour around a vertical pile exposed to waves for different KC numbers. Finally, the validated model is used to simulate scour around the jacket structure. Based on the analysis of the simulated results, the following conclusions can be drawn:

In the case of wave-induced scour around a pile, the scour depth is seen to be increasing four times with KC in the range $6 \leq \text{KC} \leq 12$. An equilibrium scour depth is achieved. The scour profile is seen to be asymmetric where the maximum scour is observed at the upstream side of the pile. The change in the maximum scour depth with KC showed a satisfactory match with the experimental data from Sumer et al. (1992). In the case of scour around the pile exposed to a steady current, the maximum scour depth is found to be S/D = -0.70. The scour topography, temporal variation of the process and the maximum scour show a good match with experimental data from Link (2006). The results demonstrate the accuracy of the model in simulating scour under waves and current.

The validated model for scour around a monopile under waves and current is applied to simulate scour around a jacket structure. The changes in the velocity profile due to wave action and a steady current are discussed. Finally, the development of the resulting scour profiles and the temporal variation of the process are presented. The maximum scour depth is calculated to be S/D = -0.70. In the case of the jacket exposed to a steady current, the maximum scour depth is found to be S/D = -0.80. The results support the field observation of the averaged scour depth ranges between S/D = 0.85 - 1.35 (Bolle et al., 2010, 2012). Overall, the simulated results demonstrate a good agreement with the experimental results for scour around the jacket structure under waves and a steady current. The current study helps to better understand the hydrodynamics and the associated scour problems around the jacket structure exposed to waves.

Acknowledgements

This study is carried out under the POL- NOR/200336/95/2014 and the authors are grateful to the grants provided by the Research Council of Norway. This study is supported in part with computational resources at the Norwegian University of Science and Technology (NTNU) provided by NOTUR under project number NN2620K.

References

Afzal, M.S., Bihs, H., Kamath, A. and Arntsen, Ø.A. (2015). Three-dimensional numerical modeling of pier scour under current and waves using level-set method. *Journal of Offshore Mechanics and Arctic Engineering*, **137**(3), 032001.

Ahmad, N., Afzal, S., Bihs, H. and Arntsen, Ø.A. (2015). Three-dimensional numerical modeling of local scour around a non-slender cylinder under varying wave conditions. In: *36th IAHR World Congress, June 2015, The Netherlands*.

Ahmad, N., Bihs, H., Alagan Chella, M. and Arntsen, Ø.A. (2018*a*). Cfd modelling of arctic coastal erosion due to breaking waves. *International Journal of Offshore and Polar Engineering*, **28**(2018).

Ahmad, N., Bihs, H., Myrhaug, D., Kamath, A. and Arntsen, Ø.A. (2018*b*). Three-dimensional numerical modelling of wave-induced scour around piles in a side-by-side arrangement. *Coastal Engineering*, **138**, 132 – 151.

Ahmad, N., Bihs, H., Myrhaug, D., Kamath, A. and Arntsen, Ø.A. (2019*a*). Numerical modeling of breaking wave induced seawall scour. *Coastal Engineering*, **150**, 108 – 120. ISSN 0378-3839. 10.1016/j.oceaneng.2020.107104https://doi.org/10.1016/j.coastaleng.2019.03.010.

Ahmad, N., Bihs, H., Myrhaug, D., Kamath, A. and Arntsen, Ø.A. (2019*b*). Numerical modelling of pipeline scour under the combined action of waves and current with free-surface capturing. *Coastal Engineering*, **148**, 19 – 35. ISSN 0378-3839. 10.1016/j.oceaneng.2020.107104https://doi.org/10.1016/j.coastaleng.2019.02.008.

Ashby, S.F. and Falgout, R.D. (1996). A parallel multigrid preconditioned conjugate gradient algorithm for groundwater flow simulations. *Nuclear Science and Engineering*, **124**(1), 145–159.

Baykal, C., Sumer, B.M., Fuhrman, D.R., Jacobsen, N.G. and Fredsøe, J. (2015). Numerical investigation of flow and scour around a vertical circular cylinder. *Phil. Trans. R. Soc. A*, **373**(2033), 20140104.

Baykal, C., Sumer, B.M., Fuhrman, D.R., Jacobsen, N.G. and Fredsøe, J. (2017). Numerical simulation of scour and backfilling processes around a circular pile in waves. *Coastal Engineering*, **122**, 87 – 107. ISSN 0378-3839.

Berthelsen, P.A. and Faltinsen, O.M. (2008). A local directional ghost cell approach for incompressible viscous flow problems with irregular boundaries. *Journal of Computational Physics*, **227**, 4354–4397.

Bihs, H. (2011). Three-dimensional numerical modeling of local scouring in open channel flow. Report, Department of Hydraulic and Environmental Engineering, Norwegian University of Science and Technology, Trondheim, Norway.

Bihs, H. and Kamath, A. (2017). A combined level set/ghost cell immersed boundary representation for floating body simulations. *International Journal for Numerical Methods in Fluids*, **83**(12), 905–916.

Bihs, H., Kamath, A., Alagan Chella, M., Aggarwal, A. and Arntsen, Ø.A. (2016). A new level set numerical wave tank with improved density interpolation for complex wave hydrodynamics. *Computers & Fluids*, **140**, 191–208.

Bihs, H. and Olsen, N.R.B. (2011). Numerical modeling of abutment scour with the focus on the incipient motion on sloping beds. *Journal of Hydraulic Engineering*, **137**(10), 1287–1292.

Bolle, A., Haerens, P., Trouw, K. and Smits, J. (2010). *Scour around gravity-based wind turbine foundations - prototype measurements*, 103–114.

Bolle, A., Winter, J.D., Goossens, W., Haerens, P. and Dewaele, G. (2012). Scour monitoring around offshore jackets and gravity based foundations. In: *6th International Conference on Scour and Erosion*.

Breuer, M., Bernsdorf, J., Zeiser, T. and Durst, F. (2000). Accurate computations of the laminar flow past a square cylinder based on two different methods: lattice-boltzmann and finite-volume. *International Journal of Heat and Fluid Flow*, **21**(2), 186 – 196. ISSN 0142-727X.

Burkow, M. and Griebel, M. (2016). A full three dimensional numerical simulation of the sediment transport and the scouring at a rectangular obstacle. *Computers & Fluids*, **125**, 1–10.

Chiew, Y. and Melville, B.W. (1987). Local scour around bridge piers. *Journal of Hydraulic Research, IAHR*, **25**(1), 15–26.

Chorin, A. (1968). Numerical solution of the Navier-Stokes equations. *Mathematics of Computation*, **22**, 745–762.

Dahlberg, R. (1983). Observations of scour around offshore structures. *Canadian geotechnical journal*, **20**(4), 617–628.

Dey, S. (2003). Threshold of sediment motion on combined transverse and longitudinal sloping beds. *Journal of Hydraulic Research*, **41**(4), 405–415.

DNV (2014). Design of offshore wind turbine structures. Offshore Standard DNV- OS-J101, Det Norske Veritas AS.

Durbin, P.A. (2009). Limiters and wall treatments in applied turbulence modeling. *Fluid Dynamics Research*, **41**, 1–18.

Fuhrman, D., Baykal, C., Sumer, B., Jacobsen, N. and Fredsøe, J. (2014). Numerical simulation of wave-induced scour and backfilling processes beneath submarine pipelines. *Coastal Engineering*, **94**, 10 – 22. ISSN 0378-3839.

Higuera, P., Lara, L.J. and Losada, I.J. (2013). Realistic wave generation and active wave absorption for Navier Stokes models application to OpenFOAM. *Coast. Eng.*, **71**, 102–118.

Hunt, J. (1954). The turbulent transport of suspended sediment in open channels. In: *Proceedings of the Royal Society of London A: Mathematical, Physical and Engineering Sciences*, volume 224, 322–335. The Royal Society.

Jacobsen, N.G., Fuhrman, D.R. and Fredsøe, J. (2012). A wave generation toolbox for the open-source CFD library: Openfoam. *International Journal for Numerical Methods in Fluids*, **70**(9), 1073–1088.

Jiang, G.S. and Peng, D. (2000). Weighted ENO schemes for Hamilton-Jacobi equations. *SIAM Journal on Scientific Computing*, **21**, 2126–2143.

Jiang, G.S. and Shu, C.W. (1996). Efficient implementation of weighted ENO schemes. *Journal of Computational Physics*, **126**, 202–228.

Kamath, A., Fleit, G. and Bihs, H. (2019). Investigation of free surface turbulence damping in rans simulations for complex free surface flows. *Water*, **11**(3), 456.

Larsen, B., Fuhrman, D. and Sumer, B. (2016). Simulation of wave-plus-current scour beneath submarine pipelines. *Journal of Waterway, Port, Coastal, and Ocean Engineering*, **142**(5), 04016003.

Larsen, B.E. and Fuhrman, D.R. (2018). On the over-production of turbulence beneath surface waves in reynolds-averaged navier–stokes models. *Journal of Fluid Mechanics*, **853**, 419–460.

Liang, D. and Cheng, L. (2005). Numerical model for wave-induced scour below a submarine pipeline. *Journal of waterway, port, coastal, and ocean engineering*, **131**(5), 193–202.

Link, O. (2006). Untersuchung der Kolkung an einem schlanken zylindrischen Pfeiler in sandigem Boden. *Wasser Abwasser GWF*, **147**(6), 421–422.

Liu, M., Lu, L., Teng, B., Zhao, M. and Tang, G. (2016). Numerical modeling of local scour and forces for submarine pipeline under surface waves. *Coastal Engineering*, **116**, 275 – 288. ISSN 0378-3839.

Liu, X. and Garcia, M. (2008). Three-dimensional numerical model with free water surface and mesh deformation for local sediment scour. *Journal of Waterway, Port, Coastal and Ocean Engineering*, **134**(4), 203–217.

Lysne, D.K. (1969*a*). Movement of sand in tunnels. *Journal of the Hydraulics Division*, **95**(6), 1835–1846.

Lysne, D.K. (1969*b*). Movement of sand in tunnels. *Journal of Hydraulic Division ASCE*, **95**(6), 1835–1846.

Nakagawa, H. and Suzuki, K. (1976). Local scour around bridge pier in tidal current. *Coastal Engineering in Japan*, **19**(1), 89–100.

Naot, D. and Rodi, W. (1982). Calculation of secondary currents in channel flow. *Journal of the Hydraulics Division*, **108**(8), 948–968.

Olsen, N.R.B. (2003). Three-dimensional CFD modeling of self-forming meandering channel. *Journal of Hydraulic Engineering*, **129**(5), 366–372.

Olsen, N.R.B. and Kjellesvig, H.M. (1998). Three-dimensional numerical flow modelling for estimation of maximum local scour depth. *Journal of Hydraulic Research*, **36**(4), 579–590.

Ong, M.C., Myrhaug, D. and Hesten, P. (2013). Scour around vertical piles due to long-crested and short-crested nonlinear random waves plus a current. *Coastal Engineering*, **73**, 106 – 114.

Osher, S. and Sethian, J.A. (1988). Fronts propagating with curvature-dependent speed: algorithms based on Hamilton-Jacobi formulations. *Journal of Computational Physics*, **79**, 12–49.

Peng, D., Merriman, B., Osher, S., Zhao, H. and Kang, M. (1999). A PDE-based fast local level set method. *Journal of Computational Physics*, **155**, 410–438.

Roulund, A., Sumer, B.M., Fredsøe, J. and Michelsen, J. (2005). Numerical and experimental investigation of flow and scour around a circular pier. *Journal of Fluid Mechanics*, **534**, 351–401.

Rouse, H. (1937). Modern conceptions of the mechanics of turbulence. *Trans. ASCE*, **102**, 463–543.

Rudolph, D., Bos, K.J., Luijendijk, A., Rietema, K. and Out, J. (2004). Scour around offshore structures-analysis of field measurements. In: *Proceedings of the 2nd International Conference on Scour and Erosion*, volume 1, 400–407.

Shields, A. (1936). *Anwendungen der Ähnlichkeitsmechanik und der Turbulenzforschung auf die Geschiebebewegung.* Mitteilungen der Preuischen Versuchsanstalt für Wasser-, Erdund Schiffbau.

Shu, C.W. and Osher, S. (1988). Efficient implementation of essentially non-oscillatory shock capturing schemes. *Journal of Computational Physics*, **77**, 439–471.

Stahlmann, A. (2013). *Experimental and numerical modeling of scour at offshore wind turbines*. Ph.D. thesis, Technische Informationsbibliothek und Universitätsbibliothek Hannover (TIB).

Stahlmann, A. and Schlurmann, T. (2012). Investigations on scour development at tripod foundations for offshore wind turbines: modeling and application. *Coastal Engineering Proceedings*, **1**(33), 90.

Sumer, B.M. and Fredsøe, J. (1990). Scour below pipelines in waves. *Journal of Waterway, Port, Coastal, and Ocean Engineering*, **116**(3), 307–323.

Sumer, B.M. and Fredsøe, J. (1997). *Hydrodynamics around cylindrical structures*. World Scientific.

Sumer, B.M., Fredsøe, J. and Christiansen, N. (1992). Scour around vertical pile in waves. *Journal of waterway, port, coastal, and ocean engineering*, **118**(1), 15–31.

Sumer, B.M., Roulund, A., Fredsøe, J. and Michelsen, J. (2002*a*). Three-dimensional numerical modeling of flow and scour around a pile. In: *Proc., 1st International Conference on scour of foundations*, 795–809.

Sumer, B.M. et al. (2002*b*). *The mechanics of scour in the marine environment*, volume 17. World Scientific Publishing Company.

Tseng, M., Yen, C. and Song, C. (2000). Computation of three-dimensional flow around square and circular bridge piers. *International Journal for Numerical Methods in fluids*, **34**, 207–227.

van der Vorst, H. (1992). Bi-CGSTAB: A fast and smoothly converging variant of Bi-CG for the solution of nonsymmetric linear systems. *SIAM Journal on scientific and Statistical Computing*, **13**, 631–644.

Van Dijk, R. (1980). Experience of scour in the southern north sea. *Scour prevention techniques around offshore structures, Society for Underwater Technology, London*, 3–10.

van Rijn, L.C. (1984*a*). Sediment transport, part I: Bed load transport. *Journal of Hydraulic Engineering*, **110**(10), 1431–1456.

van Rijn, L.C. (1984*b*). Sediment transport, part II: Suspended load transport. *Journal of Hydraulic Engineering*, **110**(11), 1613–1641.

Wilcox, D.C. (1994). *Turbulence modeling for CFD*. DCW Industries Inc., La Canada, California.

Wu, W., Rodi, W. and Wenka, T. (2000). 3D numerical modeling of flow and sediment transport in open channels. *Journal of Hydraulic Engineering*, **126**(1), 4–15.

Notations

The following symbols are used in this paper:

α = transverse bed slope;
φ = angle of repose;
η = ratio of the drag force to the inertia force;
τ = bed shear stress;
τ_0 = Shields critical bed shear stress;
τ_{cr} = modified critical bed stress;
ρ = fluid density;
ρ_s = sediment density;
ν = fluid kinematic viscosity;
ν_t = eddy viscosity;
ω = specific turbulent dissipation;
$\phi(\vec{x}, t)$ = level set function;
κ = von Karman constant;
$q_{B,i}$ = bed load transport rate;
w_s = fall velocity of the sediment particles;
$\Gamma(x)$ = the relaxation function
Γ = sediment mixing coefficient;
θ = Shields parameter;
θ_c = critical Shields parameter;
λ = wavelength;
a = reference level;
d_{50} = median grain size;
g = gravitational acceleration;
i, j, k = indices representing directions along the x-, y- and z-axis;
k_s = equivalent sand roughness;
k = turbulent kinetic energy;
h = still water level;
n = sediment porosity;
p = pressure;
s = specific density;
t_s = test duration for sediment transport;
u = horizontal velocity;
z = bed-level;
D = pile diameter (m);
E = entrainment rate;
H = wave height;
KC = Keulegan-Carpenter number;
NWT = numerical wave tank;
P_k = turbulent production rate;
S = maximum scour depth;
T = wave period;
S/D = normalised maximum scour depth;